Cement and Concrete Research 156 (2022) 106787

Contents lists available at ScienceDirect

Cement and Concrete Research

journal homepage: www.elsevier.com/locate/cemconres

The first experimental evidence for improved nanomechanical properties of calcium silicate hydrate by polycarboxylate ether and graphene oxide

Jiaqi Li [a,*], Qi Zheng [b]

[a] Atmospheric, Earth, and Energy Division, Lawrence Livermore National Laboratory, CA, United States
[b] Department of Civil and Environmental Engineering, University of California, Berkeley, United States

ARTICLE INFO

Keywords:
C-S-H
PCE
GO
Nanocomposite
Bulk modulus

ABSTRACT

Graphene oxide (GO) efficiently enhances macroscale mechanical properties of cement-based materials. Yet the nanoscale reinforcing mechanism of GO for calcium silicate hydrate (C-S-H), the key binding phase of concrete, remains poorly understood. Moreover, how polycarboxylate ether (PCE)-based superplasticizers affect the nanomechanical properties of C-S-H remains unclear. The intrinsic mechanical properties of the nanocomposites are measured using high-pressure X-ray diffraction. The influences of GO and PCE on the local Ca and Si environments are probed using X-ray absorption spectroscopy. For the first time, we evidence that PCE-induced well-dispersed GO nanoplatelets strengthen the C-S-H basal planes, whereas poorly water-dispersed GO weakly interacts with basal planes and does not strengthen in plane Ca—O bonds. Both PCE and GO only slightly strengthen C-S-H's c-axis. The bulk modulus of C-S-H/PCE/GO nanocomposite is 190% than pure C-S-H. Functional groups of PCE and GO prefer interacting with the Ca—O sheets of C-S-Hs instead of silicate tetrahedra.

1. Introduction

Nanomaterials are common additives for modifying the mechanical properties, durability, and rheology of cement-based materials [1]. The addition of nanomaterials, including but not limited to calcium silicate hydrate (C–S–H) seeds, nanosilica, nanoclay, and carbon nanotubes, in cement-based materials have been extensively studied [2,3]. Graphene and graphene oxide (GO) are among the hottest topics in materials science due to their supreme properties, e.g., large surface area (1500+ m^2/g) with two-dimensional morphology and high intrinsic in-plane Young's modulus (380–470 GPa for GO) at the nanoscale (defect-free level) [4,5]. Their use is trendy in scientific research of cement-based materials and alkali-activated materials [7–9]. Recent advances in research and development of graphene and GO manufactures result in scalable production and lower cost, making their use in concrete practical and scalable [10–12].

Graphene is a single atomic layer of graphite, consisting of sp^2 bonded carbon atoms arranged in a hexagonal lattice [13,14]. GO is the oxidized form of graphene with functional groups (e.g., carbonyl, epoxy, hydroxyl, and carboxyl) [15]. The GO incorporation in binder matrixes is more favorable relative to the graphene incorporation due to the stronger interactions between cement pastes and GO functional groups [16]. The addition of GO in cement-based materials results in improved tensile and compressive strengths due to a refined microstructure of pastes [17–19]. The strength improvement is more pronounced when GO nanoplatelets are dispersed by superplasticizers, typically polycarboxylate ether (PCE)-based [20]. A nanoindentation study has showed that the addition of GO does not enhance the microscale Young's modulus of C-S-H (the primary binding phase of concrete) [21]. In contradiction, molecular dynamics simulations have indicated GO-strengthened C-S-Hs at the nanoscale [22]. There remains a gap between understanding the micro- and nano-scale influences of GO on the C-S-H mechanical properties. The nanoscale mechanical properties of C-S-H in the presence of GO need to be experimentally validated. Measuring the nanomechanical properties of GO-incorporated C-S-H is important, yet challenging. Additionally, the influences of comb-shaped PCE (a hotly studied and widely used superplasticizer) on the nanomechanical properties of C-S-Hs are still poorly understood.

High-pressure X-ray diffraction (HP-XRD) is a powerful tool to determine the intrinsic mechanical properties of (nano)crystalline phases [23–25]. In HP-XRD experiments, the microstructure influences (e.g., mesopores and crystal size) on nanomechanical properties measurement can be eliminated by filling pressure-transmitting medium into the mesopores. Thus, hydrostatic pressures can be applied onto C-S-

* Corresponding author.
E-mail address: li88@llnl.gov (J. Li).

https://doi.org/10.1016/j.cemconres.2022.106787
Received 1 October 2021; Received in revised form 10 February 2022; Accepted 22 March 2022
Available online 10 April 2022

H nanocrystallites, and their nanomechanical properties can be measured at the scale of unit cells. HP-XRD has been successfully applied to determine the influences of Ca-to-Si molar ratio (Ca/Si) [26], Al incorporation [27], cross-linking structures [28], synthesis method [29], and decalcification [30] on the intrinsic mechanical properties of nanocrystalline C-S-Hs.

In this study, a pure nanocrystalline C-S-H reference and C-S-H-based nanocomposites with the additions of GO and PCE are synthesized. The influences of GO and PCE additions on the coordination environment of Ca and Si of C-S-H are studied using X-ray absorption near-edge fine structure (XANES) spectroscopy. The intrinsic mechanical properties of C-S-H and PCE/GO incorporated C-S-H nanocomposites are investigated using HP-XRD. The nanomechanical properties of the nanocomposites are correlated to their nanostructure, and the PCE-GO synergic effect is evidenced. The GO reinforcing mechanism of nanocrystalline C-S-Hs is unveiled. The mild PCE reinforcing effect on C-S-H is reported. The results have great potential in optimizing GO incorporated cement-based or alkali-activated materials for buildings, oil-cementing, and carbon storage capping when inexpensive GO is largely available. Our results are also valuable for validating nanoscale simulation of binary and ternary systems of C-S-H, PCE, and GO, as well as providing the first-hand data to develop forcefields of molecular dynamics for understanding C-S-H's interaction with polymers and GO.

2. Materials and methods

2.1. Materials and synthesis

Pure C–S–H (the reference group) was synthesized at an initial Ca/Si of 1.0 using the co-precipitation method [29]. Stoichiometric amounts of $Na_2SiO_3{\cdot}9H_2O$ (99+%, Fisher) and $Ca(NO_3)_2{\cdot}4H_2O$ (99+%, Fisher) were separately dissolved in 250 mL deionized water in two 500 mL HDPE bottles in a N_2-filled glovebox at 25 °C. The water to solid precursors ($Na_2SiO_3{\cdot}9H_2O$ and $Ca(NO_3)_2{\cdot}4H_2O$) mass ratio was 50. Na_2SiO_3 solution was continuously dropped into $Ca(NO_3)_2$ solution, immediately forming a white slurry. The initial pH of the suspension in the pure C–S–H system was 12.03. The sealed bottles were shaken at 60 rpm for seven days at 25 °C. Subsequently, the slurry was filtered using 0.45 μm nylon membranes with a vacuum pump (flow rate 37 L/min, Millipore Sigma) under N_2 protection. The remnant gel-like product was vacuum-dried for seven days at 25 °C with the presence of 10 g NaOH pellets (97+%, Fisher) in a 10.5 L glass desiccator to minimize carbonation.

C–S–H-based nanocomposites, C–S–H/GO, C–S–H/PCE, and C–S–H/PCE/GO, were synthesized also using the co-precipitation method, but with the addition of GO, PCE, and a PCE-GO mixture, respectively. GO was synthesized using the modified Hummers method [31]. A comb-shaped PCE with a molecular weight of 36,000 g/mol [32] was used in this study. The number of side chains (molecular weight 1000 g/mol) in one molecule is 27. The carboxylate to ether ratio is 2.67. The number of ethylene oxide monomers in one side chain is 23. For C-S-H/PCE synthesis, the PCE solution (30 wt%) was dropped into a 250 mL $Ca(NO_3)_2$ solution. The rest of mixing protocol of C-S-H/PCE system followed the C-S-H synthesis. Before curing for seven days, the system pH was adjusted to 12.03 by dropping 174 μL of 1 N NaOH solution (FisherSci).

The GO used in this study has been characterized earlier in [33]. No additional phase was found in this batch. Our GO contains 10% of carboxyl and 15% of carbonyl groups on the plane edges. The core region of GO with an O/C molar ratio of 0.23 contains 60% hydroxyl and 40% epoxy groups. The intrinsic (nanoscale) Young's modulus of GO depends on the degree of oxidation [4]. For the used GO with O/C = 0.23 in our experimental study of nanomechanical properties of C-S-H nanocomposites, its Young's modulus is ~410 GPa. The GO aqueous solution (15 mg/mL) was ultra-sonicated for 10 min before the nanocomposite synthesis. The mixing protocol of nanocomposites considerably impacts their dispersion and further properties [34]. GO immediately agglomerated in the Na_2SiO_3 solution in our trial mix because GO hardly stabilizes in highly alkaline environments, consistent with existing literature [34]. Thus, for the synthesis of C-S-H/GO, GO solution was added into $Ca(NO_3)_2$ solution, followed by 10 min ultra-sonication. Na_2SiO_3 solution was then dropped into GO-$Ca(NO_3)_2$ solution, followed by pH adjustment to 12.03 by the addition of 900 μL of 1 N NaOH solution. For the synthesis of C-S-H/PCE/GO, PCE solution was first mixed with $Ca(NO_3)_2$ solution. GO solution was then dropped into the PCE-$Ca(NO_3)_2$ solution, followed by 10 min ultra-sonication. Na_2SiO_3 solution was then dropped into the PCE-GO-$Ca(NO_3)_2$ solution, followed by pH adjustment to 12.03 by adding 1180 μL of 1 N NaOH solution. The rest of synthesis protocol of C-S-H/GO and C-S-H/PCE/GO both followed the aforementioned C-S-H reference synthesis. The PCE solid content to precursor mass ratio of the C–S–H/PCE and C–S–H/PCE/GO systems was both 4.9%. This PCE dose was also used in previous studies to simulate the high superplasticizer to C-S-H ratio during the early age of cement hydration when the PCE adsorption and dispersion are effective [35]. Similarly, the GO solid dose to precursor mass ratio of the C–S–H/GO and C–S–H/PCE/GO systems was both 1.5% to mimic the early age cement hydration in the presence of GO.

2.2. X-ray absorption near-edge fine structure spectroscopy

The XANES spectra of the C–S–H and C–S–H-based nanocomposites at the Ca $L_{2,3}$-edge were collected using the scanning transmission X-ray microscopy at the bend beamline 5.3.2.2 of the Advanced Light Source (ALS) at the Lawrence Berkeley National Laboratory. The energy step of each scan was 0.1 eV. The experimental setup is detailed in [36]. The XANES spectra at the Si K-edge were collected at the PHOENIX beamline of the Swiss Light Source at Paul Scherrer Institute, Switzerland. The data were collected using a fluorescence-yield mode with a 500 μm × 500 μm beam at room temperature. The spectra were recorded at an energy step of 0.15 eV for 1 s for each data point. More experimental details can be found in [37].

2.3. High-pressure X-ray diffraction

The HP-XRD experiment was conducted at the superbend beamline 12.2.2 of the ALS. A BX90 diamond anvil cell was used for pressurizing the samples. A 250 μm thick rhenium gasket was pre-indented to ~100 μm thick by the diamond anvil pair. A 110 μm diameter cylindrical chamber was laser-milled at the indent center. Each powder sample was loaded into the chamber, followed by the blending with 1–3 ruby microspheres [23]. The chamber was filled with pressure-transmitting medium (ethanol-methanol solution at 1:4 volume ratio) before an immediate closure with the diamond anvil pair. The applied hydrostatic pressure to the sample was determined by an offline fluorescence station. The size of the X-ray beam (wavelength 0.4959 Å) was ~30 μm × 30 μm. Diffraction patterns at elevated hydrostatic pressure and at ambient pressure were collected from the chamber and sample-filled silica capillaries, respectively. The diffraction peaks were fitted using Marquardt fitting method with PVII type in XFIT [38]. Celref [39] was used to refine the B11m tobermorite structure [40] in the pressure range of 0–~10 GPa.

Biot strain of a C-S-H unit cell is defined as:

$$\text{Biot strain} = \frac{l - l_0}{l_0} \tag{1}$$

where l and l_0 are the measured and ambient pressure lattice lengths, respectively.

The second-order Birch-Murnaghan equation of state (Eq. (2)) describes the correlation between bulk modulus and the pressure-induced volumetric change of a C-S-H unit cell.

$$P = \frac{3}{2}K_0\left[(1-\varepsilon \mathrm{V})^{-\frac{7}{3}} - (1-\varepsilon \mathrm{V})^{-\frac{5}{3}}\right] \tag{2}$$

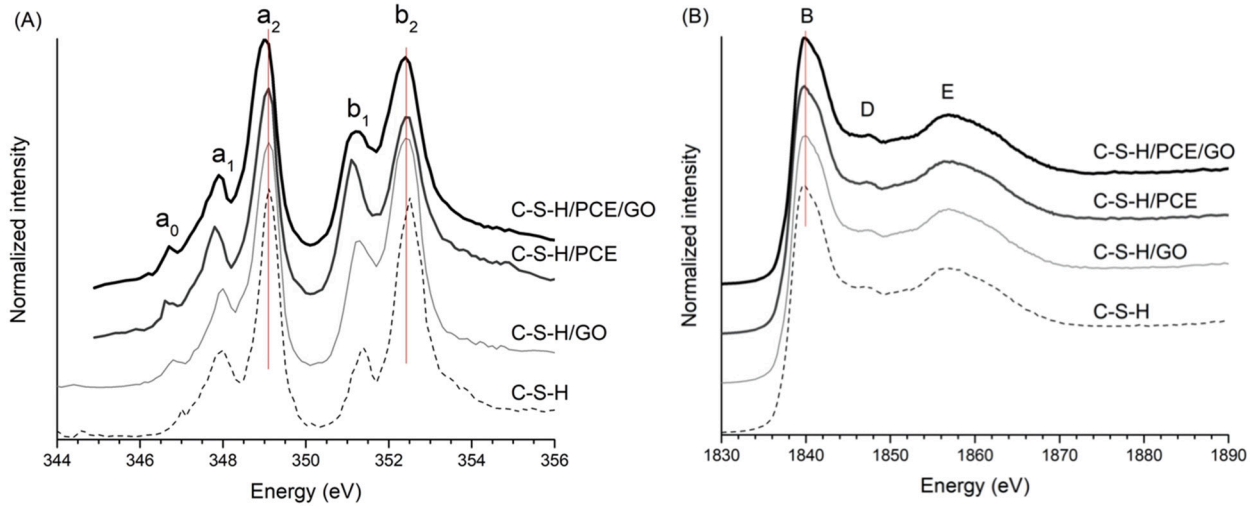

Fig. 1. XANES spectra of C-S-H and C-S-H-based composites at (A) Ca $L_{2,3}$-edge; (B) at Si K-edge. The splitting energies, ΔL_3 and ΔL_2, of C-S-H, C-S-H/GO, C-S-H/PCE, and C-S-H/PCE-GO are 1.08 eV and 1.08 eV, 1.1 eV and 1.14 eV, 1.24 eV and 1.27 eV, 1.11 eV and 1.17 eV, respectively.

where P is the applied hydrostatic pressure (GPa) to a unit cell, ε_V (unitless) is the volumetric strain of a unit cell, and K_0 (GPa) is the bulk modulus of a unit cell at ambient pressure.

3. Results and discussion

3.1. Ca and Si coordination environments

Fig. 1A shows the XANES spectra of the C-S-H and C-S-H-based composites at the Ca $L_{2,3}$-edge.

The spectra result from the electron transition from 2p to 3d orbitals of Ca [41]. Two major peaks, a_2 and b_2, originate from the loss of degeneracy of 2p orbitals ($2p_{3/2}$ and $2p_{1/2}$) by spin-orbit coupling. Minor peaks (a_1 and b_1) are observed at the left of each major peak due to crystal field splitting [42]. The leading peak a_0 corresponds to the mixing of states due to the 3d spin-orbit splitting effect and multipole interactions of core holes with valence electrons. The b_2 peaks of C-S-H/GO and C-S-H/PCE are positioned at 0.05 eV lower energy compared to the b_2 peak of C-S-H. The a_2 and b_2 peak energies are 0.1 eV and 0.03 eV, respectively, lower than those of C-S-H/GO and C-S-H/PCE. Note that the a_2 and b_2 peak energies of C-S-Hs are very sensitive to Ca—O coordination and typically vary in a short range, within 0.1 eV [36]. Thus, the a_2 and b_2 peak shift of C-S-H nanocomposites, although not noticeable, can be an index for the variation in coordination environment (e.g., coordination number of Ca) of C-S-H-based materials. The energy shift suggests that the addition of PCE and/or GO induces a smaller mean coordination number of Ca [29], i.e., more CaO sheets are six-fold coordinated in the C-S-H-based nanocomposites compared to the well-accepted CaO_7 sheet in C-S-H.

The energy differences (splitting energies, $\Delta L_3 = a_2 - a_1$ and $\Delta L_2 = b_2 - b_1$) of the two doublets between the adjacent minor and major peaks depend on the distortion of octahedral-like symmetry of Ca—O [43]. The splitting energies are very sensitive to the degree of distortion of Ca—O. The splitting energies of pure C-S-H without structural modifications only vary from 1.05 to 1.15 eV [36]. The low splitting energy, 1.08 eV, of the C-S-H reference suggests the typical distorted octahedral symmetry in interlayer Ca and CaO_7 sheets of C-S-H [44]. The splitting energies of C-S-H/PCE are 1.24 and 1.27 eV, out of the C-S-H range 1.05–1.15 eV. Although the splitting energies of C-S-H/PCE are only over 0.16 eV higher than those of the C-S-H reference, the high sensitivity of splitting energy suggesting a higher degree of octahedral symmetry around Ca (less distorted [45]) in C-S-H/PCE due to the strong interaction between CaO sheets and COO^- groups of PCE [46]. The splitting energies of C-S-H/GO are 0.02–0.06 eV higher than the reference, suggesting a slightly higher degree of octahedral symmetry around Ca in C-S-H/GO relative to C-S-H due to 1) the low availability of COO^- groups on GO edges; 2) week interactions between Ca of C-S-H and the hydroxyl and epoxy groups of GO [16]; and 3) low surface area of agglomerated GO nanoplatelets in a basic environment (pH = 12) [47,34]. Ca in C-S-H/PCE/GO exhibits a slightly higher degree of octahedral symmetry compared to C-S-H/GO due to the interactions between CaO sheets and the PCE-induced well-dispersed GO nanoplatelets [34].

Table 1
Compositions and lattice parameters of C-S-H and C-S-H-based nanocomposites.

	Final Ca/Si[a]	*a* (Å)	*b* (Å)	*c* (Å)	V ($Å^3$)	Basal spacing (Å)
C-S-H	0.91	6.691 ± 0.01	7.308 ± 0.01	25.0 ± 0.1	1030	12.52
C-S-H/GO	0.84	6.670 ± 0.01	7.300 ± 0.01	24.7 ± 0.1	1014	12.34
C-S-H/PCE	0.95	6.697 ± 0.01	7.301 ± 0.01	24.8 ± 0.1	1024	12.41
C-S-H/PCE/GO	0.86	6.681 ± 0.01	7.288 ± 0.01	25.4 ± 0.1	1036	12.70

[a] Ca/Si was measured using Bruker SuperX energy-dispersive X-ray spectroscopy detector.

Si K-edge XANES spectra of the C-S-H and C-S-H-based composites are shown in Fig. 1B. The major peak B (Si K-edge) at ~1839.8 eV is attributed to the dipole-allowed transition of 1s electrons to 3p orbital of Si [48]. The post-edge humps D at ~1847. 5 eV and E in an energy range of 1845–1855 eV correspond to the multiple-scattering effect from more distant coordination shells and the 1s-3d electron transition of Si, respectively. The Si K-edge energy is very sensitive to the silicate polymerization degree of tobermorite-like phases (e.g., C-S-H) [36,37]. The variation in Si K-edge energy of C-S-H with various degrees of silicate polymerization is 1.5 eV. Thus, the low variation (<0.12 eV) of Si K-edge energy among our four C-S-H and nanocomposite samples suggests a comparable degree of silicate polymerization and poor interaction between the additives and C-S-H silicate tetrahedron. The addition of PCE and/or GO exhibits negligible influences on the silicate mean chain length because 1) the additives prefer interacting with CaO sheets; and 2) the interactions between the silicate tetrahedra and GO epoxy and hydroxyl groups are more favorable in the presence of bridging Ca at higher Ca/Si ratios [8]. The poor interaction between the additives and

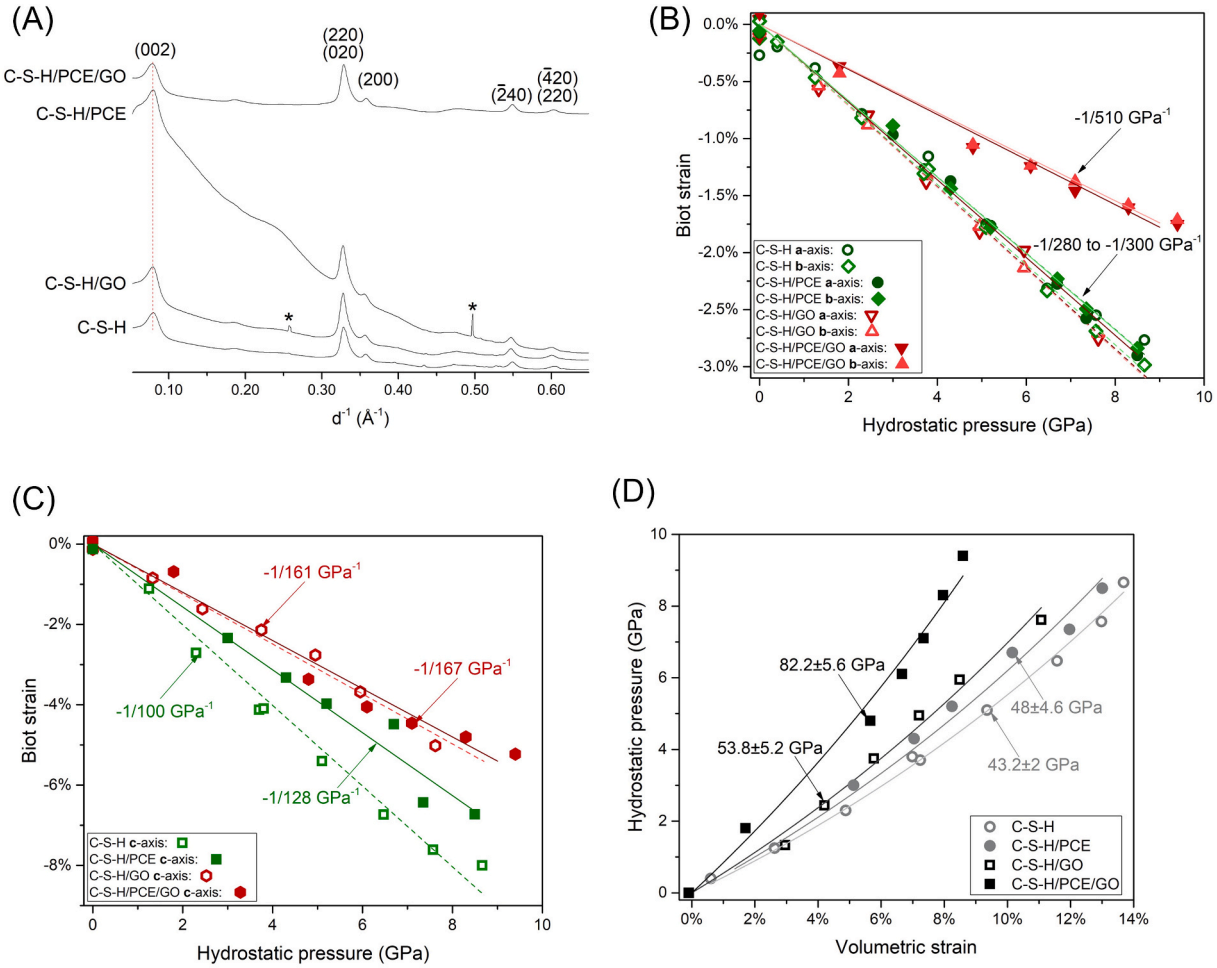

Fig. 2. (A) X-ray diffractogram of the samples; asterisks indicate the diffraction of capillary impurities; (B) Biot strain as a function of applied hydrostatic pressure along the a- and b-axis; axial incompressibility is indicated by fitted-lines; (C) along the c-axis; (D) bulk modulus K_0 by fitting the second order Birch-Murnaghan equation of state. The uncertainty of the Biot stain is <0.2%. The estimated uncertainty of applied hydrostatic pressure is 0.1 GPa.

silicate tetrahedra can be explained by the lack of bridging functionality (e.g., silyl groups) of the additives [46].

3.2. Nanomechanical properties

The final Ca/Si and lattice parameters of the samples are listed in Table 1. The final Ca/Si of nanocomposites slightly increases in the presence of comb-shaped PCE, which is consistent with [49]. The slight reduction of final Ca/Si in the presence of GO may be related to the Ca complexation with GO functional groups [50]. The additions of PCE and GO exhibit negligible influences on lattice parameters *a* and *b*. The low variation in basal spacing (see 002 peak position in Fig. 2A) indicates that PCE and GO are unlikely to intercalate into interlayers.

Fig. 2B shows the axial incompressibility of the samples along the a- and b-axis of unit cells. Biot strain is more negative with an increasing applied hydrostatic pressure due to the pressure-induced contraction of unit cells. The incompressibility of C-S-H reference, C-S-H/PCE, and C-S-H/GO along the a- and b-axis is in the range of $-1/280$ GPa^{-1} to $-1/300$ GPa^{-1}, which falls in the typical range for C-S-Hs [26–29] and tobermorite [51]. The comparable ab-plane (basal plane) incompressibilities of C-S-H, C-S-H/PCE, and C-S-H/GO suggest that neither GO nor PCE separately reinforces the C-S-H basal planes. The ab-plane incompressibility of C-S-H/PCE/GO is about $-1/510$ GPa^{-1}. The basal plane of C-S-H/PCE/GO is the stiffest among all known tobermorite and C-S-H-based phases [26–30,51]. The in-plane Young's modulus is very high, 210–470 GPa [5]. This fact suggests that PCE-well-dispersed GO nanoplatelets flank and reinforce C-S-H basal planes, whereas poorly water-dispersed GO weakly interacts with basal planes and do not strengthen in-plane Ca—O bonds.

Fig. 2C shows the incompressibility of the samples along the c-axis (normal to the basal plane). The incompressibility of the C-S-H reference along the c-axis is -100 GPa^{-1}, suggesting a relatively soft c-axis. The c-axis of the C-S-H reference with final Ca/Si = 0.91 is stiffer than that of C-S-H at Ca/Si = 0.8 ($-1/94$ GPa^{-1}) [29] and softer than that of C-S-H at Ca/Si = 1.3 ($-1/193$ GPa^{-1}), following the negative correlation between c-axis incompressibility and Ca/Si ratio. The c-axis of the three nanocomposites is just slightly stiffer than that of the C-S-H reference because 1) the c-axis incompressibility is governed by interlayer density [29] and 2) PCE- and/or GO-modified CaO sheets are possibly stiffer along the c-axis (i.e., Ca—O bonds along the c-axis are slightly stronger).

Fig. 2D shows the measured bulk modulus, K_0, of C-S-H and C-S-H-based nanocomposites at the unit cell level. K_0 of the C-S-H reference (final Ca/Si = 0.91) is 43.2 ± 2 GPa, suggesting a relatively soft C-S-H nanostructure. This value is higher than 40 GPa of C-S-H at Ca/Si = 0.8 and lower than 64.6 GPa of C-S-H at Ca/Si = 1.3, following the negative correlation between K_0 and Ca/Si of nanocrystalline C-S-Hs [29]. The K_0 of C-S-H/PCE and C-S-H/GO nanocomposites are 48 ± 4.6 GPa and 53.8 ± 5.2 GPa, respectively. Their slightly higher K_0 relative to the reference can be explained by the comparable ab-planar incompressibility and the slightly stiffer c-axis. C-S-H/PCE/GO's significantly higher ab-planar incompressibility ($-1/510$ GPa^{-1}) and the slightly stiffer c-axis explain its high bulk modulus, 82.2 ± 5.6 GPa, confirming the

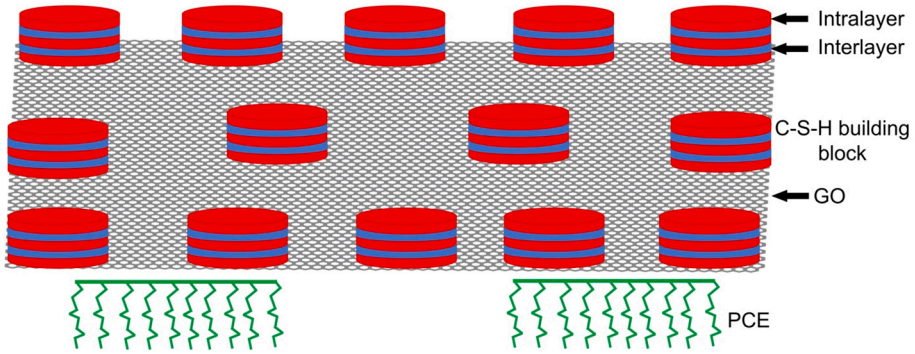

Fig. 3. A schematic of C-S-H, PCE, and GO interaction in C-S-H/PCE/GO nanocomposites. The green combs indicate PCE, a grey mesh represents a GO nanoplatelet, and red and blue alternating stacked layers of the C-S-H building blocks represent the intralayer and interlayer, respectively. (For interpretation of the references to color in this figure legend, the reader is referred to the web version of this article.)

reinforcing effect of PCE-dispersed GO nanoplatelets. This value is higher than K_0 of all tobermorite, Al-tobermorite, C-S-Hs, and calcium aluminate hydrates measured in our previous studies [26,28,29,51,52]. Thus, the well-dispersed GO in the presence of PCE can strengthen C-S-H at the nanoscale is evidenced.

Fig. 3 illustrates the nanoscale interactions among C-S-H building blocks (nano globules), GO nanoplatelets, and comb-shaped PCE based on the results of C-S-H/PCE/GO. PCE disperses GO nanoplatelets and the steric stabilization of PCE reduces the agglomeration of GO [34]. Well-dispersed GO nanoplatelets are templates for the nucleation and growth of C-S-H building blocks. The CaO sheets of intralayers interact with the functional groups of GO, reorganizing the coordination environment of intralayer Ca instead of that of Si. Thus, the basal planes of C-S-Hs are aligned and reinforced along the a- and b-axis by PCE-dispersed GO nanoplatelets.

4. Conclusions

This study presents synchrotron radiation-based material characterizations of nanocrystalline C-S-H and PCE- and/or GO-modified C-S-H nanocomposites at Ca/Si of ~1.0. The intrinsic mechanical (nanomechanical) properties of the C-S-H-based samples at the unit cell level are measured. The key conclusions are:

- The intralayer Ca of C-S-H weakly interacts with the functional groups in the presence of only PCE or GO. The interactions between intralayer Ca and GO are strong in the presence of a PCE-GO mixture. CaO sheets are more six-fold coordinated and less distorted in the C-S-H/PCE/GO nanocomposite.
- PCE, GO, and the PCE-GO mixture all prefer interactions with Ca rather than Si. Neither PCE nor GO exhibits pronounced influences on the coordination environment of Si of the nanocomposites. The influences of the functional groups on the lattice parameters of all samples are relatively low.
- In the presence of only PCE or GO, the basal planes of C-S-H are not reinforced, while only the c-axis is slightly strengthened. The bulk moduli of C-S-H/PCE and C-S-H/GO increase by up to 24% compared to the pure C-S-H reference.
- In the presence of the PCE-GO mixture, the basal planes are significantly stiffer, while the c-axis is only slightly strengthened. The bulk modulus of C-S-H/PCE/GO is 90% higher than that of the C-S-H reference due to the PCE-GO synergic effect. PCE-dispersed GO nanoplatelets significantly reinforce C-S-H basal planes.

The results provide the first experimental evidence for the reinforcement of C-S-H with PCE-GO at the nanoscale. This study provides new insight into the reinforcing mechanism of PCE-GO for C-S-H building blocks and the nanostructure of C-S-H-based nanocomposites. Therefore, this work has great implications in designing GO-reinforced cement-based or alkali-activated materials in service and understanding the interactions between PCE and cement.

CRediT authorship contribution statement

Jiaqi Li: Conceptualization, Methodology, Investigation, Validation, Visualization, Writing - original draft, Funding acquisition.
Qi Zheng: Investigation, Validation, Writing - review & editing.

Declaration of competing interest

The authors declare that they have no known competing financial interests or personal relationships that could have appeared to influence the work reported in this paper.

Acknowledgements

We thank Dr. Jinyuan Yan's, Dr. Martin Kunz's, and Dr. Matthew Marcus's technical support at the ALS. The Advanced Light Source is supported by the Director, Office of Science, Office of Basic Energy Sciences, of the U.S. Department of Energy under Contract DE-AC02-05CH11231. Dr. Sunxiang Zheng at Baoxia Mi's group at Berkeley is thanked for offering the GO samples. Dr. Delphine Marchon at ETH Zürich and Berkeley is thanked for the PCE. We thank Dr. Paulo Monteiro for sharing beamtime at SLS. We thank Wenxin Zhang at Caltech for plotting Fig. 2. We acknowledge the Paul Scherrer Institut, Villigen, Switzerland for provision of synchrotron radiation beamtime at beamline PHOENIX of the SLS and would like to thank Dr. Thomas Huthwelker for assistance. This work was performed under the auspices of the U.S. Department of Energy by Lawrence Livermore National Laboratory under Contract DE-AC52-07NA27344. IM release number is: LLNL-JRNL-826909.

References

[1] K. Sobolev, I. Flores, R. Hermosillo, L.M. Torres-Martínez, Nanomaterials and nanotechnology for high-performance cement composites, in: Proceedings of ACI Session on Nanotechnology of Concrete: Recent Developments and Future Perspectives, 2006, pp. 91–118.
[2] P.J.M. Monteiro, G.Q. Geng, D. Marchon, J.Q. Li, P. Alapati, K.E. Kurtis, M.J. A. Qomi, Advances in characterizing and understanding the microstructure of cementitious materials, Cem. Concr. Res. 124 (2019), 105806.
[3] P. Bost, M. Regnier, M. Horgnies, Comparison of the accelerating effect of various additions on the early hydration of Portland cement, Constr. Build. Mater. 113 (2016) 290–296.
[4] L. Liu, J. Zhang, J. Zhao, F. Liu, Mechanical properties of graphene oxides, Nanoscale 4 (2012) 5910–5916.
[5] S. Ghazizadeh, P. Duffour, N.T. Skipper, Y. Bai, Understanding the behaviour of graphene oxide in Portland cement paste, Cem. Concr. Res. 111 (2018) 169–182.

[7] X. Zhu, X. Kang, J. Deng, K. Yang, L. Yu, C. Yang, A comparative study on shrinkage characteristics of graphene oxide (GO) and graphene nanoplatelets (GNPs) modified alkali-activated slag cement composites, Mater. Struct. 54 (2021) 1–15.
[8] M. Izadifar, J.S. Dolado, P. Thissen, A. Ayuela, Interactions between reduced graphene oxide with monomers of (calcium) silicate hydrates: a first-principles study, Nanomaterials 11 (2021) 2248.
[9] X. Kang, X. Zhu, J. Liu, X. Shu, J. Qian, Y. Huang, Hydration of C3A/gypsum composites in the presence of graphene oxide, Mater. Today Commun. 23 (2020), 100889.
[10] D.X. Luong, K.V. Bets, W.A. Algozeeb, M.G. Stanford, C. Kittrell, W. Chen, R. V. Salvatierra, M. Ren, E.A. McHugh, P.A. Advincula, Gram-scale bottom-up flash graphene synthesis, Nature 577 (2020) 647–651.
[11] B. Liu, J. Xie, H. Ma, X. Zhang, Y. Pan, J. Lv, H. Ge, N. Ren, H. Su, X. Xie, From graphite to graphene oxide and graphene oxide quantum dots, Small 13 (2017) 1601001.
[12] N. Muradov, Low to near-zero CO2 production of hydrogen from fossil fuels: status and perspectives, Int. J. Hydrog. Energy 42 (2017) 14058–14088.
[13] A.K. Geim, Graphene: status and prospects, Science 324 (2009) 1530–1534.
[14] S.M. Clark, K.J. Jeon, J.Y. Chen, C.S. Yoo, Few-layer graphene under high pressure: Raman and X-ray diffraction studies, Solid State Commun. 154 (2013) 15–18.
[15] Y. Zhu, S. Murali, W. Cai, X. Li, J.W. Suk, J.R. Potts, R.S. Ruoff, Graphene and graphene oxide: synthesis, properties, and applications, Adv. Mater. 22 (2010) 3906–3924.
[16] D. Hou, Z. Lu, X. Li, H. Ma, Z. Li, Reactive molecular dynamics and experimental study of graphene-cement composites: structure, dynamics and reinforcement mechanisms, Carbon 115 (2017) 188–208.
[17] K. Gong, Z. Pan, A.H. Korayem, L. Qiu, D. Li, F. Collins, C.M. Wang, W.H. Duan, Reinforcing effects of graphene oxide on Portland cement paste, J. Mater. Civil Eng. 27 (2015).
[18] X.H. Zhu, X.J. Kang, K. Yang, C.H. Yang, Effect of graphene oxide on the mechanical properties and the formation of layered double hydroxides (LDHs) in alkali-activated slag cement, Constr. Build. Mater. 132 (2017) 290–295.
[19] X. Kang, X. Zhu, J. Qian, J. Liu, Y. Huang, Effect of graphene oxide (GO) on hydration of tricalcium silicate (C3S), Construction and Building Materials 203 (2019) 514–524.
[20] Y. Xu, J. Zeng, W. Chen, R. Jin, B. Li, Z. Pan, A holistic review of cement composites reinforced with graphene oxide, Constr. Build. Mater. 171 (2018) 291–302.
[21] W. Long, Y. Gu, B. Xiao, Q. Zhang, F. Xing, Micro-mechanical properties and multi-scaled pore structure of graphene oxide cement paste: synergistic application of nanoindentation, X-ray computed tomography, and SEM-EDS analysis, Constr. Build. Mater. 179 (2018) 661–674.
[22] P. Wang, G. Qiao, Y. Guo, Y. Zhang, D. Hou, Z. Jin, J. Zhang, M. Wang, X. Hu, Molecular dynamics simulation of the interfacial bonding properties between graphene oxide and calcium silicate hydrate, Constr. Build. Mater. 260 (2020), 119927.
[23] J. Li, W. Zhang, P.J. Monteiro, Mechanical properties of struvite-K: a high-pressure X-ray diffraction study, Cem. Concr. Res. 136 (2020), 106171.
[24] J. Moon, S. Kim, S. Bae, S.M. Clark, Pressure-induced anomalous behavior of thaumasite crystal, J. Am. Ceram. Soc. 103 (2020) 3763–3775.
[25] J. Moon, S. Yoon, R.M. Wentzcovitch, S.M. Clark, P.J.M. Monteiro, Elastic properties of tricalcium aluminate from high-pressure experiments and first-principles calculations, J. Am. Ceram. Soc. 95 (2012) 2972–2978.
[26] G. Geng, R.J. Myers, M.J.A. Qomi, P.J.M. Monteiro, Densification of the interlayer spacing governs the nanomechanical properties of calcium-silicate-hydrate, Sci. Rep. 7 (2017) 10986.
[27] J. Li et al., The nanomechanical properties of non-crosslinked calcium aluminosilicate hydrate: the influences of tetrahedral Al and curing age, Cement and Concrete Research, (Under Review).
[28] G. Geng, R.J. Myers, J. Li, R. Maboudian, C. Carraro, D.A. Shapiro, P.J. Monteiro, Aluminum-induced dreierketten chain cross-links increase the mechanical properties of nanocrystalline calcium aluminosilicate hydrate, Sci. Rep. 7 (2017) 44032.
[29] J. Li, W. Zhang, P.J.M. Monteiro, The structure and intrinsic mechanical properties of nanocrystalline calcium silicate hydrate, ACS Sustain. Chem. Eng. 8 (2020) 12453–12461.
[30] L. Liu, C. Sun, G. Geng, P. Feng, J. Li, R. Dahn, Influence of decalcification on structural and mechanical properties of synthetic calcium silicate hydrate (C-S-H), Cem. Concr. Res. 123 (2019).
[31] M. Hu, B. Mi, Enabling graphene oxide nanosheets as water separation membranes, Environ. Sci. Technol. 47 (2013) 3715–3723.
[32] C. Li, J. Li, A. Telesca, D. Marchon, K. Xu, M. Marroccoli, Z. Jiang, P.J. Monteiro, Effect of polycarboxylate ether on the expansion of ye'elimite hydration in the presence of anhydrite, Cem. Concr. Res. 140 (2021), 106321.
[33] S. Zheng, Q. Tu, J.J. Urban, S. Li, B. Mi, Swelling of graphene oxide membranes in aqueous solution: characterization of interlayer spacing and insight into water transport mechanisms, ACS Nano 11 (2017) 6440–6450.
[34] Z. Lu, A. Hanif, C. Ning, H. Shao, R. Yin, Z. Li, Steric stabilization of graphene oxide in alkaline cementitious solutions: mechanical enhancement of cement composite, Mater. Des. 127 (2017) 154–161.
[35] A. Popova, G. Geoffroy, M.F. Renou-Gonnord, P. Faucon, E. Gartner, Interactions between polymeric dispersants and calcium silicate hydrates, J. Am. Ceram. Soc. 83 (2000) 2556–2560.
[36] J. Li, G. Geng, R. Myers, Y.S. Yu, D. Shapiro, C. Carraro, R. Maboudian, P.J. M. Monteiro, The chemistry and structure of calcium (alumino) silicate hydrate: a study by XANES, ptychographic imaging, and wide- and small-angle scattering, Cem. Concr. Res. 115 (2019) 367–378.
[37] J. Li, W. Zhang, K. Garbev, P.J. Monteiro, Coordination environment of Si in calcium silicate hydrates, silicate minerals, and blast furnace slags: a XANES database, Cem. Concr. Res. 143 (2021), 106376.
[38] R. Cheary, A. Coelho, Programs XFIT and FOURYA, deposited in CCP14 powder diffraction library, in: Engineering and Physical Sciences Research Council, Daresbury Laboratory, Warrington, England, 1996.
[39] J. Laugier, B. Bochu, V. Celref, Developed at the Laboratoire des Matériaux et du Génie Physique, Ecole Nationale Supérieure de Physique de Grenoble (INPG), 2003.
[40] S. Merlino, E. Bonaccorsi, T. Armbruster, The real structure of tobermorite 11 angstrom: normal and anomalous forms, OD character and polytypic modifications, Eur. J. Miner. 13 (2001) 577–590.
[41] S. Bae, R. Taylor, D. Hernandez-Cruz, S. Yoon, D. Kilcoyne, P.J.M. Monteiro, Soft X-ray spectromicroscopic investigation of synthetic C-S-H and C3S hydration products, J. Am. Ceram. Soc. 98 (2015) 2914–2920.
[42] J. Li, W. Zhang, K. Xu, P.J.M. Monteiro, Fibrillar calcium silicate hydrate seeds from hydrated tricalcium silicate lower cement demand, Cem. Concr. Res. 137 (2020), 106195.
[43] G. Geng, J. Li, Y.-S. Yu, D.A. Shapiro, D.A. Kilcoyne, P.J. Monteiro, Nanometer-resolved spectroscopic study reveals the conversion mechanism of CaO·Al2O3·10H2O to 2CaO·Al2O3·8H2O and 3CaO·Al2O3·6H2O at an elevated temperature, Cryst. Growth Des. 17 (2017) 4246–4253.
[44] J. Li, G. Geng, W. Zhang, Y.S. Yu, D.A. Shapiro, P.J.M. Monteiro, The hydration of beta- and alpha(H)'-dicalcium silicates: an X-ray spectromicroscopic study, ACS Sustain. Chem. Eng. 7 (2019) 2316–2326.
[45] G.Q. Geng, R. Taylor, S. Bae, D. Hernandez-Cruz, D.A. Kilcoyne, A.H. Emwas, P.J. M. Monteiro, Atomic and nano-scale characterization of a 50-year-old hydrated C3S paste, Cem. Concr. Res. 77 (2015) 36–46.
[46] C.A. Orozco, B.W. Chun, G. Geng, A.H. Emwas, P.J. Monteiro, Characterization of the bonds developed between calcium silicate hydrate and polycarboxylate-based superplasticizers with silyl functionalities, Langmuir 33 (2017) 3404–3412.
[47] X.Y. Li, Y.M. Liu, W.G. Li, C.Y. Li, J.G. Sanjayan, W.H. Duan, Z.J. Li, Effects of graphene oxide agglomerates on workability, hydration, microstructure and compressive strength of cement paste (vol 145, pg 402, 2017), Constr. Build. Mater. 179 (2018) 537–538.
[48] D. Li, G.M. Bancroft, M.E. Fleet, X.H. Feng, Silicon K-edge Xanes spectra of silicate minerals, Phys. Chem. Miner. 22 (1995) 115–122.
[49] V. Kanchanason, J. Plank, Role of pH on the structure, composition and morphology of C-S-H-PCE nanocomposites and their effect on early strength development of Portland cement, Cem. Concr. Res. 102 (2017) 90–98.
[50] A. Sabziparvar, E. Hosseini, V. Chiniforush, A. Korayem, Barriers to achieving highly dispersed graphene oxide in cementitious composites: an experimental and computational study, Constr. Build. Mater. 199 (2019) 269–278.
[51] J. Li, W. Zhang, K. Garbev, G. Beuchle, P.J. Monteiro, Influences of cross-linking and Al incorporation on the intrinsic mechanical properties of tobermorite, Cem. Concr. Res. 136 (2020), 106170.
[52] G. Geng, J. Li, Y. Zhou, L. Liu, J. Yan, M. Kunz, P.J.M. Monteiro, A high-pressure X-ray diffraction study of the crystalline phases in calcium aluminate cement paste, Cem. Concr. Res. 108 (2018) 38–45.

Further Reading

[6] S. Chuah, Z. Pan, J.G. Sanjayan, C.M. Wang, W.H. Duan, Nano reinforced cement and concrete composites and new perspective from graphene oxide, Constr. Build. Mater. 73 (2014) 113–124.